# Intraluminal laser speckle rheology using an omni-directional viewing catheter

JING WANG,[1,3] MASAKI HOSODA,[1,2,3] DIANE M. TSHIKUDI,[1] ZEINAB HAJJARIAN,[1] AND SEEMANTINI K. NADKARNI[1,*]

[1]*Wellman Center for Photomedicine, Harvard Medical School and Massachusetts General Hospital, MA 02114, USA*
[2]*Healthcare Optics Research Laboratory, Canon U.S.A., Inc., Cambridge, MA 02139, USA*
[3]*Authors contributed equally to this work*
[*]*snadkarni@mgh.harvard.edu*

**Abstract:** A number of disease conditions in luminal organs are associated with alterations in tissue mechanical properties. Here, we report a new omni-directional viewing Laser Speckle Rheology (LSR) catheter for mapping the mechanical properties of luminal organs without the need for rotational motion. The LSR catheter incorporates multiple illumination fibers, an optical fiber bundle and a multi-faceted mirror to permit omni-directional viewing of the luminal wall. By retracting the catheter using a motor-drive assembly, cylindrical maps of tissue mechanical properties are reconstructed. Evaluation conducted in a test phantom with circumferentially-varying mechanical properties demonstrates the capability of the LSR catheter for the accurate mechanical assessment of luminal organs.

## References and links

1. M. O'Rourke, "Mechanical principles in arterial disease," Hypertension **26**(1), 2–9 (1995).
2. L. H. Arroyo and R. T. Lee, "Mechanisms of plaque rupture: mechanical and biologic interactions," Cardiovasc. Res. **41**(2), 369–375 (1999).
3. S. Suresh, J. Spatz, J. P. Mills, A. Micoulet, M. Dao, C. T. Lim, M. Beil, and T. Seufferlein, "Connections between single-cell biomechanics and human disease states: gastrointestinal cancer and malaria," Acta Biomater. **1**(1), 15–30 (2005).
4. G. Sommer, *Mechanical Properties of Healthy and Diseased Human Arteries*, Monographic Series TU Graz: Computation in Engineering and Science (Verlag der Techn. Univ. Graz, 2010).
5. P. D. Richardson, "Biomechanics of plaque rupture: progress, problems, and new frontiers," Ann. Biomed. Eng. **30**(4), 524–536 (2002).
6. G. S. Soor, I. Vukin, S. W. Leong, G. Oreopoulos, and J. Butany, "Peripheral vascular disease: who gets it and why? A histomorphological analysis of 261 arterial segments from 58 cases," Pathology **40**(4), 385–391 (2008).
7. T. G. Mason and D. A. Weitz, "Optical measurements of frequency-dependent linear viscoelastic moduli of complex fluids," Phys. Rev. Lett. **74**(7), 1250–1253 (1995).
8. S. K. Nadkarni, B. E. Bouma, T. Helg, R. Chan, E. Halpern, A. Chau, M. S. Minsky, J. T. Motz, S. L. Houser, and G. J. Tearney, "Characterization of atherosclerotic plaques by laser speckle imaging," Circulation **112**(6), 885–892 (2005).
9. S. K. Nadkarni, A. Bilenca, B. E. Bouma, and G. J. Tearney, "Measurement of fibrous cap thickness in atherosclerotic plaques by spatiotemporal analysis of laser speckle images," J. Biomed. Opt. **11**(2), 021006 (2006).
10. S. K. Nadkarni, B. E. Bouma, D. Yelin, A. Gulati, and G. J. Tearney, "Laser speckle imaging of atherosclerotic plaques through optical fiber bundles," J. Biomed. Opt. **13**(5), 054016 (2008).
11. Z. Hajjarian, J. Xi, F. A. Jaffer, G. J. Tearney, and S. K. Nadkarni, "Intravascular laser speckle imaging catheter for the mechanical evaluation of the arterial wall," J. Biomed. Opt. **16**(2), 026005 (2011).
12. Z. Hajjarian and S. K. Nadkarni, "Evaluating the viscoelastic properties of tissue from laser speckle fluctuations," Sci. Rep. **2**, 316 (2012).
13. Z. Hajjarian and S. K. Nadkarni, "Evaluation and correction for optical scattering variations in laser speckle rheology of biological fluids," PLoS One **8**(5), e65014 (2013).
14. M. M. Tripathi, Z. Hajjarian, E. M. Van Cott, and S. K. Nadkarni, "Assessing blood coagulation status with laser speckle rheology," Biomed. Opt. Express **5**(3), 817–831 (2014).
15. Z. Hajjarian and S. K. Nadkarni, "Correction of optical absorption and scattering variations in Laser Speckle Rheology measurements," Opt. Express **22**(6), 6349–6361 (2014).

16. Z. Hajjarian, M. M. Tripathi, and S. K. Nadkarni, "Optical Thromboelastography to evaluate whole blood coagulation," J. Biophotonics **8**(5), 372–381 (2015).

17. D. Weitz and D. Pine, "Diffusing-wave spectroscopy," in *Dynamic Light Scattering.*, W. Brown, ed. (Oxford Univ. Press, 1993), pp.652–721.

18. T. G. Mason, H. Gang, and D. A. Weitz, "Diffusing-wave-spectroscopy measurements of viscoelasticity of complex fluids," J. Opt. Soc. Am. A **14**(1), 139–149 (1997).

19. B. R. Dasgupta and D. A. Weitz, "Microrheology of cross-linked polyacrylamide networks," Phys. Rev. E Stat. Nonlin. Soft Matter Phys. **71**(2), 021504 (2005).

20. B. Berne and R. Pecora, *Dynamic Light Scattering: With Applications to Chemistry, Biology, and Physics* (John Wiley & Sons, 2000).

21. S. K. Nadkarni, "Optical measurement of arterial mechanical properties: from atherosclerotic plaque initiation to rupture," J. Biomed. Opt. **18**(12), 121507 (2013).

22. S. K. Nadkarni, B. E. Bouma, J. de Boer, and G. J. Tearney, "Evaluation of collagen in atherosclerotic plaques: the use of two coherent laser-based imaging methods," Lasers Med. Sci. **24**(3), 439–445 (2009).

23. S. K. Nadkarni, J. D. Toussaint, G. J. Tearney, and Z. Hajjarian, "Intracoronary laser speckle imaging (ILSI) for the mechanical characterization of coronary plaques in living swine," presented at SPIE Photonics West San Francisco, California, United States, 21–26 January 2012.

24. S. K. Nadkarni, J. D. Toussaint, and Zeinab. Hajjarian, "Intravascular laser speckle imaging (ILSI): in vivo evaluation of the mechanical properties of coronary plaques in living swine," presented at SPIE European Conference on Biomedical Optics, Munich, Germany, 22–26 May 2011.

25. Z. Hajjarian and S. K. Nadkarni, "Laser speckle micro-rheology for biomechanical evaluation of breast tumors," Proc. SPIE **9710**, 9710–9717 (2016).

26. W. W. Ong, "Laser Speckle Imaging for the characterization of cartilage," Boston University (2010).

27. G. J. Tearney, S. A. Boppart, B. E. Bouma, M. E. Brezinski, N. J. Weissman, J. F. Southern, and J. G. Fujimoto, "Scanning single-mode fiber optic catheter-endoscope for optical coherence tomography," Opt. Lett. **21**(7), 543–545 (1996).

28. J. Wang and S. K. S. K. Nadkarni, "The influence of optical fiber bundle parameters on the transmission of laser speckle patterns," Opt. Express **22**(8), 8908–8918 (2014).

29. "Dow Corning product information Dow Corning® 184 silicone elastomer," http://www.dowcorning.com/DataFiles/090276fe80190b08.pdf.

30. "Bio-Rad handcasting Polyacrylamide gels protocol 6201," http://www.bio-rad.com/webroot/web/pdf/lsr/literature/Bulletin_6201.pdf.

31. A. Revzin, R. J. Russell, V. K. Yadavalli, W.-G. Koh, C. Deister, D. D. Hile, M. B. Mellott, and M. V. Pishko, "Fabrication of poly(ethylene glycol) hydrogel microstructures using photolithography," Langmuir **17**(18), 5440–5447 (2001).

32. C.-Y. Lee and J.-H. Han, "Integrated spatio-spectral method for efficiently suppressing honeycomb pattern artifact in imaging fiber bundle microscopy," Opt. Commun. **306**, 67–73 (2013).

33. D. J. Pine, D. A. Weitz, P. M. Chaikin, and E. Herbolzheimer, "Diffusing wave spectroscopy," Phys. Rev. Lett. **60**(12), 1134–1137 (1988).

34. D. J. Pine, D. A. Weitz, J. X. Zhu, and E. Herbolzheimer, "Diffusing-wave spectroscopy: dynamic light scattering in the multiple scattering limit," J. Phys. **51**(18), 2101–2127 (1990).

35. D. A Weitz, J. X. Zhu, D. J. Durian, and D. J. Pine, "Principles and applications of diffusing-wave spectroscopy," in *Structure Dynamics of Strongly Interacting Colloids Supramolecular Aggregates in Solution*, S.-H. Chen, J. S. Huang, and P. Tartaglia, eds. (Springer, 1992) pp. 731–748.

36. "D. A Weitz, J. X. Zhu, D. J. Durian, H. Gang, and D. J. Pine, "Diffusing-wave spectroscopy: The technique and some applications," Phys. Scr. T **49B**, 610–621 (1993).

37. G. Maret, "Diffusing-wave spectroscopy," Curr. Opin. Colloid Interface Sci. **2**(3), 251–257 (1997).

38. A. Banchio, G. Nägele, and J. Bergenholtz, "Viscoelasticity and generalized Stokes–Einstein relations of colloidal dispersions," J. Chem. Phys. **111**(18), 8721–8740 (1999).

39. T. G. Mason, "Estimating the viscoelastic moduli of complex fluids using the generalized Stokes-Einstein equation," Rheol. Acta **39**(4), 371–378 (2000).

40. J. L. Harden and V. Viasnoff, "Recent advances in DWS-based micro-rheology," Curr. Opin. Colloid Interface Sci. **6**(5-6), 438–445 (2001).

41. S. K. Kumar, G. Szamel, and J. F. Douglas, "Nature of the breakdown in the Stokes-Einstein relationship in a hard sphere fluid," J. Chem. Phys. **124**(21), 214501 (2006).

42. Z. Hajjarian and S. K. Nadkarni, "Estimation of particle size variations for laser speckle rheology of materials," Opt. Lett. **40**(5), 764–767 (2015).

43. J. Lauger and H. Stettin, "Effects of instrument and fluid inertia in oscillatory shear in rotational rheometers," J. Rheo. **60**(3), 393–406 (2016).

44. B. F. Kennedy, R. A. McLaughlin, K. M. Kennedy, L. Chin, A. Curatolo, A. Tien, B. Latham, C. M. Saunders, and D. D. Sampson, "Optical coherence micro-elastography: mechanical-contrast imaging of tissue microstructure," Biomed. Opt. Express **5**(7), 2113–2124 (2014).

45. C. Sun, B. Standish, and V. X. D. Yang, "Optical coherence elastography: current status and future applications," J. Biomed. Opt. **16**(4), 043001 (2011).

46. S. Wang and K. V. Larin, "Optical coherence elastography for tissue characterization: a review," J. Biophotonics

**8**(4), 279–302 (2015).

47. L. F. Rojas-Ochoa, S. Romer, F. Scheffold, and P. Schurtenberger, "Diffusing wave spectroscopy and small-angle neutron scattering from concentrated colloidal suspensions," Phys. Rev. E Stat. Nonlin. Soft Matter Phys. **65**(5), 051403 (2002).

48. J. X. Zhu, D. J. Durian, J. Müller, D. A. Weitz, and D. J. Pine, "Scaling of transient hydrodynamic interactions in concentrated suspensions," Phys. Rev. Lett. **68**(16), 2559–2562 (1992).

49. D. A. Weitz, D. J. Pine, P. N. Pusey, and R. J. Tough, "Nondiffusive Brownian motion studied by diffusing-wave spectroscopy," Phys. Rev. Lett. **63**(16), 1747–1750 (1989).

50. W. van Megen and P. N. Pusey, "Dynamic light-scattering study of the glass transition in a colloidal suspension," Phys. Rev. A **43**(10), 5429–5441 (1991).

51. H. J. van Staveren, C. J. M. Moes, J. van Marie, S. A. Prahl, and M. J. C. van Gemert, "Light scattering in intralipid-10% in the wavelength range of 400–1100 nm," Appl. Opt. **30**(31), 4507–4514 (1991).

52. M. H. Kao, A. G. Yodh, and D. J. Pine, "Observation of Brownian motion on the time scale of hydrodynamic interactions," Phys. Rev. Lett. **70**(2), 242–245 (1993).

53. R. K. Chhetri, K. A. Kozek, A. C. Johnston-Peck, J. B. Tracy, and A. L. Oldenburg, "Imaging three-dimensional rotational diffusion of plasmon resonant gold nanorods using polarization-sensitive optical coherence tomography," Phys. Rev. E Stat. Nonlin. Soft Matter Phys. **83**(4), 040903 (2011).

54. H. Ullah, A. Mariampillai, M. Ikram, and I. A. Vitkin, "Can temporal analysis of optical coherence tomography statistics report on dextrorotatory-glucose levels in blood?" Laser Phys. **21**(11), 1962–1971 (2011).

55. S. Haavisto, A. I. Koponen, and J. Salmela, "New insight into rheology and flow properties of complex fluids with Doppler optical coherence tomography," Front Chem. **2**, 27 (2014).

56. H. Ullah, B. Davoudi, A. Mariampillai, G. Hussain, M. Ikram, and I. A. Vitkin, "Quantification of glucose levels in flowing blood using M-mode swept source optical coherence tomography," Laser Phys. **22**(4), 797–804 (2012).

57. X. Liang, A. L. Oldenburg, V. Crecea, E. J. Chaney, and S. A. Boppart, "Optical micro-scale mapping of dynamic biomechanical tissue properties," Opt. Express **16**(15), 11052–11065 (2008).

58. M. J. Gora, J. S. Sauk, R. W. Carruth, K. A. Gallagher, M. J. Suter, N. S. Nishioka, L. E. Kava, M. Rosenberg, B. E. Bouma, and G. J. Tearney, "Tethered capsule endomicroscopy enables less invasive imaging of gastrointestinal tract microstructure," Nat. Med. **19**(2), 238–240 (2013).

## 1. Introduction

A number of disease conditions including coronary atherosclerosis, peripheral artery disease and gastrointestinal neoplasms are associated with alterations in tissue mechanical properties [1–6]. For instance, acute myocardial infarction (AMI), the leading cause of death worldwide, is caused by the rupture of mechanically-compromised atherosclerotic plaques [2,5]. Fibrotic stiffening and calcification of peripheral arteries may cause obstructive stenosis impairing blood flow to the extremities [6]. In gastro-intestinal neopasms, tumor stiffness may be associated with malignant transformation [3]. Thus, the evidence on the role of mechanical factors in disease progression calls for the development of novel technologies for evaluating tissue mechanical properties to improve detection and diagnostic yield.

Laser speckle rheology (LSR) is a new optical approach that can quantify the mechanical properties of materials in a non-contact manner by analyzing the temporal fluctuations of laser speckle intensities [7–16]. In viscoelastic materials, laser speckle, resulting from the interference of multiply scattered coherent light, is modulated in time by the Brownian motion of light scattering particles, and the extent of particle motion is in turn governed by the viscoelastic susceptibility of the microenvironment surrounding the particles [7,8,11–21]. In prior work, LSR has been successfully applied to measure tissue mechanical properties for addressing a number of biomedical and clinical questions that include the mechanical characterization of coronary plaques [8–11,22–24], the quantification of blood coagulation status in patients [14,16], the detection of mechanical features of benign and malignant tumors [25], and the characterization of the viscoelastic properties of human osteoarthritic knee cartilage [26]. LSR has also been extensively demonstrated in complex biofluids and test phantom materials encompassing a large range of mechanical moduli (over 6 decades) and optical properties [13,15].

The majority of LSR studies thus far have been conducted *ex vivo* or under *in vitro* conditions. In order to evaluate the mechanical properties of tissues beyond sub-surface locations, and within deep, inaccessible fields and geometries, LSR must be conducted via a miniature endoscope or catheter, capable of delivering light to internal organs in a minimally-

invasive manner. We have previously demonstrated a miniaturized side-viewing catheter (1.5 mm diameter) for the intraluminal assessment of tissue viscoelasticity [11,23,24]. Intravascular testing in the aortas of living animals demonstrated the capability for quantifying arterial mechanical properties even under the conditions of cardiac motion and respiration [11,23,24]. The diagnostic capability of this previous device however, was limited, because it recovered an indirect index of tissue viscoelasticity via the time constant, $\tau$, of the temporal speckle intensity autocorrelation, $g_2(t)$, and could do so only at discrete locations without the capability for circumferential mapping of the coronary vessel lumen [11,23,24].

While the time constant, $\tau$, provides an indirect assessment of sample viscoelasticity [8–10,22], material properties are best defined by the frequency-dependent, viscoelastic modulus, $G^*(\omega)$, that quantifies the solid-like and fluid-like behavior of materials over a deformation frequency, $\omega$. Furthermore, to facilitate comprehensive evaluation of luminal organs, the capability for circumferential mapping of tissue mechanical properties during catheter pull-back is necessary. Therefore, in this paper, we describe a new intra-luminal LSR catheter that quantifies the viscoelastic modulus, $G^*(\omega)$, and also enables cylindrical mapping of luminal organs without the need for catheter rotation. To test the performance of the LSR catheter, we prepared a gel phantom with mechanical moduli that vary in both circumferential and longitudinal directions. The cylindrical maps of phantom viscoelastic moduli were reconstructed that demonstrated the capability of the LSR catheter for intra-luminal and omni-directional mechanical characterization. Using conventional mechanical rheometry as a reference standard, we report on the accuracy of this new omni-directional LSR approach.

## 2. Material and methods

### 2.1 Omni-directional LSR catheter

The conventional approach for circumferential viewing of luminal organs is by mechanically rotating an optical fiber attached to a side-facing mirror or prism within an external sheath during imaging, as for instance in optical coherence tomography (OCT) [27]. However, to conduct LSR via a catheter, an optical fiber bundle (OFB) with thousands of optical cores transmits laser speckle patterns reflected from the lumen wall [10,11]. Since each core of the OFB supports multiple propagating modes, mechanical rotation could increase mode coupling between neighboring optical cores and unpredictably modulate the transmitted speckle patterns [10,28]. To overcome this limitation, we describe a new approach to accomplish omni-directional LSR by using multiple single-mode fibers (SMF) and a customized multi-faceted pyramidal mirror (MFPM) [Fig. 1(a)] to guide light to various circumferential locations on the lumen wall and simultaneously collect multiple laser speckle patterns, thus circumventing the need for mechanical rotation.

The MFPM was fabricated by polishing the tip of a multimode optical fiber at angles of 48° to allow oblique viewing and avoid specular reflections from the catheter sheath and lumen wall. The average roughness of the polished mirror surfaces measured using an interferometer (NewView6300, Zygo) was 13 nm, which was better than or comparable with commercially available 1" mirrors. In addition, the MFPM was coated with 99.99% aluminum using an evaporator (DV-502A, Denton) to enhance reflectivity. MFPM's of diameters 800μm and 600 μm with four and six facets were fabricated for incorporation within the LSR catheter [Fig. 1(a)]. The field of view (FOV) of the LSR probe measured using an Air Force chart was 53° in the circumferential direction and 25° in the longitudinal direction for each MFPM facet. This was equivalent to a circumferential coverage of 59% for the 4-faceted and 89% for the 6-faceted MFPM, respectively. The results presented here were obtained using the 4-faceted MFPM catheter assembly.
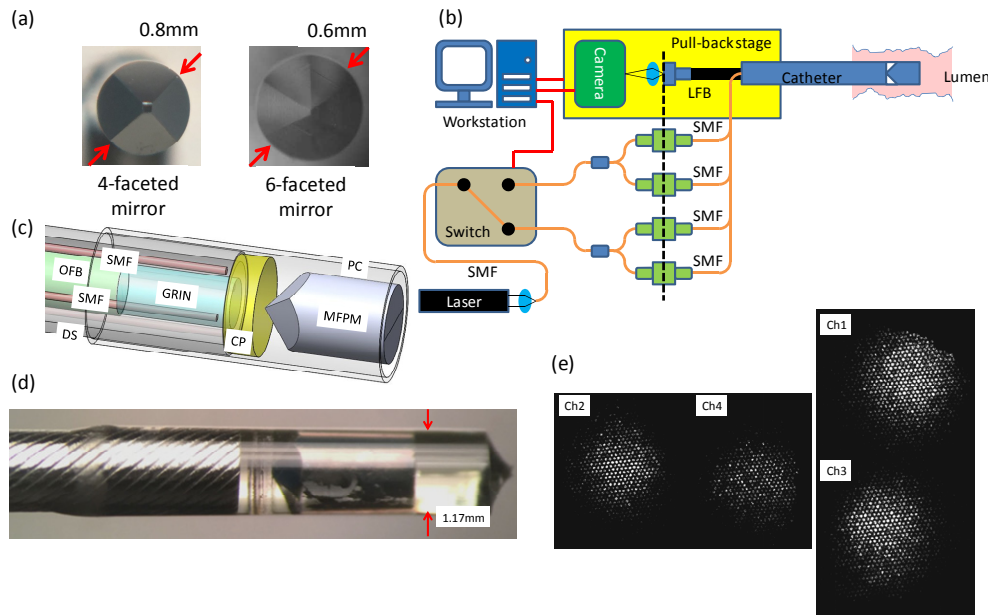
Fig. 1. Omni-directional LSR catheter assembly. The design of the distal optics is optimized for a lumen of 3 mm diameter (size of a human coronary artery). (a) The top view of the 4-faceted and 6-faceted MFPMs. (b) The schematic diagram of the omni-directional LSR catheter, pull-back assembly and console hardware. Laser light (633 nm, 22.5mW), coupled into a single mode fiber (SMF) passes through a MEMS switch, and is split to 4 illumination fibers. The speckle patterns obtained from the lumen wall are transmitted through an optical fiber bundle (OFB) and are imaged on the CMOS camera. (c) The computer aided drawing shows the catheter distal optics assembly which incorporates single mode fibers (SMFs) for illumination, a circular polarizer (CP), a multi-faceted pyramidal mirror (MFPM), a gradient-index (GRIN) lens, and an optical fiber bundle (OFB). The distal assembly is housed within a protective polycarbonate (PC) tube and a customized drive shaft (DS). (d) The photograph of the distal optic assembly. The catheter diameter is 1.2mm. (e) Representative speckle images obtained from 4 catheter channels (mirror facets), with two opposite channels acquired simultaneously.

The schematic diagram of the LSR system including the omni-directional LSR catheter, a pull-back assembly and console hardware are shown in Fig. 1(b). Light from a He-Ne laser (Thorlabs, 633nm wavelength, 22.5mW) was coupled into the input of a MEMS optical switch (OSW12-633E, Thorlabs) through an SMF. Each of the two outputs of the MEMS switch was connected to an input of a 2-by-2 fiber coupler (Thorlabs) that equally divided light into 2 custom-manufactured SMFs of reduced diameter (OFS, 80 µm in diameter). The 4 SMFs ran parallel with a leached optical fiber bundle (Schott USA; 3500 cores and 0.55 mm in diameter) and delivered light to the distal end of the catheter to illuminate the lumen wall. The 4 SMFs were precisely aligned with the custom-fabricated MFPM [Fig. 1(c)] so that each SMF only illuminated one of the multiple mirror facets. The speckle patterns from the lumen wall, reflected off the MFPM facets, were imaged on the distal face of the OFB through a Gradient-index (GRIN) lens [Figs. 1(a) and 1(b)]. In prior work we observed that an OFB with a large core-core separation is required to reduce speckle modulation caused by light coupling between optical cores [10,28]. Therefore, in this study, a leached OFB with core diameter of 4.5 µm and core-core distance of 7.4 µm was used to permit robust speckle pattern transmission [28]. A custom-manufactured circular polarizer (CP) disk laser-cut from a circular polarizing film (thickness = 300 µm) was used to reduce specular reflections from the catheter sheath and to isolate depolarized, multiply-scattered light. The MFPM and CP were incorporated within a polycarbonate (PC) tube filled with an optically-transparent, degassed epoxy to protect the distal optics from external stress. The PC tube containing the

assembled distal optics was then attached to a drive shaft (ASAHI INTECC) that housed the GRIN lens, the illumination fibers, and the OFB [Fig. 1(d)]. During imaging, the drive shaft containing the catheter assembly was pulled back through a transparent protective sheath. A motor drive unit (MDU) (ILS200PP, Newport) controlled by a motor controller (ESP 301, Newport) was used to accomplish catheter pull-back in discrete steps over a maximum pull-back distance of 20 cm. A high speed CMOS camera (MC1310, Mikrotron) for capturing laser speckle patterns at high frame rates (up to 2 kHz) was directly housed on the MDU and the proximal face of the OFB was imaged on the CMOS sensor using a 40X objective lens [Fig. 1(b)]. The CMOS camera was interfaced with the imaging workstation via a CameraLink frame grabber (Karbon CL2-F, BitFlow).

To facilitate omni-directional imaging, the MEMS switch was used to avoid speckle image overlap. In particular, to obtain a large field of view (FOV) over a small optical working distance (~2 mm), the optical stop of the distal optical assembly is located on the surface of the GRIN lens, and not on the MFPM facets. Therefore, the speckle images reflected from the neighboring mirror facets could overlap on the end face of the OFB causing erroneous results. To avoid potential image overlap, speckle patterns were instead acquired from two opposite facets at a time (CH1 and CH3 in Fig. 1(e)). Following acquisition, illumination was rapidly switched to the other two opposing facets (CH2 and CH4) using the MEMS optical switch. Using this approach, circumferential-scanning of the illumination spot was achieved and speckle patterns omni-directionally collected from the lumen wall without the need for mechanical rotation. Software for controlling image acquisition, MDU motion and illumination switching in real-time was developed in C + + by exploiting multi-threading parallel processing.

## 2.2 Gel phantom preparation

The performance of the LSR catheter was evaluated using a custom-developed, cylindrical test phantom with mechanical moduli that vary in both circumferential and longitudinal directions, as shown in Fig. 2. Fabrication of the phantom was accomplished using 3 different materials of distinct mechanical properties: Polydimethylsiloxane (PDMS), Polyethylene Glycol (PEG) and Polyacrylamide (PA).
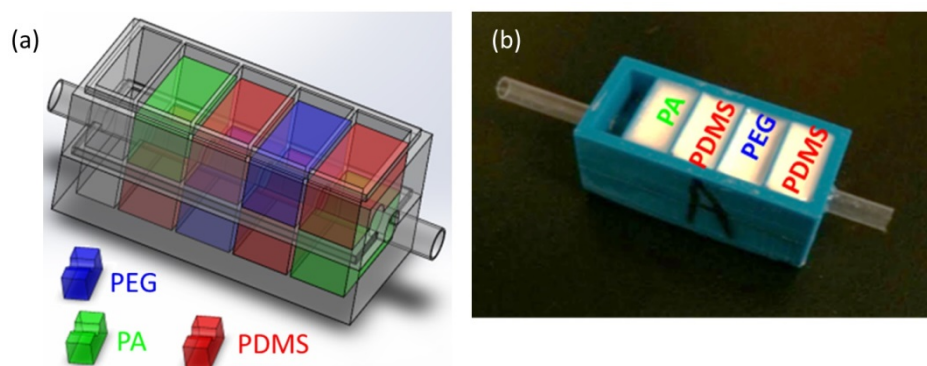


Fig. 2. (a) CAD design and (b) photograph of 8-cell phantom with varying mechanical properties and identical optical properties. The dimension of each cell is 14x7x7mm (Width × Length × Depth). The blue, green and red blocks represent the PEG gel ($|G*|$~18 Pa), PA gel ($|G*|$~77 Pa) and PDMS gel ($|G*|$~9.5 kPa), respectively. $G*$ values are reported at a rheometer oscillation frequency of 1Hz.

PDMS gels were prepared using the Sylgard 184 silicone elastomer kit (Dow Corning) by mixing the base and curing agent in 10:1 ratios as per the manufacturer's specifications and curing the mixture at room temperature for 12 hours [29]. The PA gels were made by co-polymerizing 3.458%v/v acrylamide (Sigma-Aldrich) and 0.042%v/v bisacrylamiden (Sigma-

Aldrich) using 0.5%v/v ammonium persulfate (Sigma-Aldrich) as the initiator and 0.1%v/v tetramethylethylenediamine (TEMED, Sigma-Aldrich) as the activator and curing for 4 hours at room temperature [30]. The PEG gels were prepared by mixing 4%v/v PEG diacrylate (Sigma-Aldrich) with 1%v/v 2-Hydroxy-2-methylpropiophenone (Sigma-Aldrich) as a photo-initiator and curing for 10 minutes under UV light [31]. Since the gels were optically clear, 0.6%w/v Titanium Dioxide ($TiO_2$) microspheres (Sigma-Aldrich) and 50%/30% intralipid (LIPOSYN II 10%, Hospira Inc.) were added into PDMS gels and PA/PEG gels, respectively, to permit light scattering and facilitate the measurement of speckle patterns. In all cases, the reduced scattering coefficient was maintained the same for all gels ($\mu'_s \sim 5mm^{-1}$) to mimic high scattering of most luminal tissues [13].

Next, an 8-cell phantom mould shown in Fig. 2 was designed and printed using a 3D printer (Replicator 2, Makerbot). Each cell was alternatively filled with PEG, PA or PDMS gel materials of distinct mechanical moduli. At the centre of the phantom mould, a clear FEP tube (3.7-mm-diameter) was used to create a lumen. As a result, the viscoelastic moduli of the luminal phantom varied in both circumferential and longitudinal directions for each gel compartment shown in Fig. 2. The gel materials were prepared to mimic viscoelastic moduli values of tissue components such as lipid-rich or necrotic tissue (~50-100Pa) and fibrous (~10-50kPa) tissue relevant to luminal tissues including human coronary arteries.

### 2.3 Mechanical testing

An AR-G2 rheometer (TA Instruments) was used for measuring the frequency-dependent viscoelastic modulus, $G^*(\omega)$, of each gel material deposited in the phantom. The gel materials for rheometry measurements were prepared as above in 40 mm-diameter petri dishes and loaded between the bottom plate and a 40 mm-diameter steel parallel top plate of the rheometer. For each gel material (PDMS, PA, and PEG), the elastic modulus, $G'(\omega)$, the viscous modulus $G''(\omega)$, and the complex shear or viscoelastic modulus, $G^*(\omega)$, were measured over the frequency range of 0.1 to 10 Hz at 25 °C. The maximum frequency of 10Hz was selected to limit effects of instrument inertia (detailed below) [43]. The strain was controlled at 1%. The magnitude of the viscoelastic modulus, $|G^*(\omega)|$ was reported for all the gel materials and compared with corresponding catheter-based LSR measurements as below.

### 2.4 Omni-directional LSR evaluation of the test phantom

To conduct intraluminal LSR, we first inserted the catheter into the phantom lumen shown in Fig. 2 and acquired time-series of speckle patterns reflected on CH1 and CH3 facets of the MFPM [Fig. 1(e)] for 2 seconds at a frame rate of 300 frames per second (fps). With the catheter at the same location, the MEMS switch was used to alternate illumination spots and a time series of speckle patterns acquired from the adjacent CH2 and CH4 facets [Fig. 1(e)]. Automated pull-back was performed to image the entire test phantom by stepping the MDU in 112 discrete steps spaced 250 µm apart. Considering a 2 s acquisition time per channel, the total imaging duration was 7.5 minutes to image a 3 cm pull-back length through the phantom. Next, the microstructure of the luminal gel phantom was imaged using a catheter-based OCT system (Lunawave, Terumo Inc). The OCT catheter was inserted into the phantom lumen and imaging was performed at a pull-back speed of 10 mm/s.

### 2.5 Omni-directional mapping of viscoelastic modulus, $G^*(\omega)$

Since the LSR catheter utilizes an OFB to transmit speckle patterns, the hexagonally assembled optical fibers create a honeycomb-like static pixilation pattern [Fig. 1(e)] [10,28,32]. To minimize this artifact, we applied a notch band reject filter for selectively eliminating the hexagonal pattern in the Fourier transform of the raw speckle images [32]. The notch reject filter was formed as the product of Butterworth high-pass filters, whose centers have been translated into the centers of each bright spot of the hexagonal pattern in Fourier domain. Then the Fourier transforms of the raw speckle images and notch band reject

filter were multiplied and recovered back to spatial domain to reconstruct pixilation-free speckle images. The transmitted speckle patterns also contained components with spatial frequencies higher than the estimated spatial frequencies of the raw speckle patterns before being transmitted through the OFB. The source of these high frequency components entailed tiny speckle spots in each multimode fiber core [10,28], which were removed by applying an additional Butterworth low pass filter.

Next, the viscoelastic modulus, $G^*(\omega)$, was calculated from time-varying speckle intensity fluctuations using previously described methods [7,12,17]. Briefly, we first calculated the intensity autocorrelation curve, $g_2(t)$, by measuring the correlation between pixel intensities in the first speckle image and the subsequent speckle image time series as follows:

$$g_2(t) = \left\langle \frac{<I(t_0)I(t_0+t)>_{\text{pixel}}}{\sqrt{<I(t_0)^2>_{\text{pixel}}}\sqrt{<I(t_0+t)^2>_{\text{pixel}}}} \right\rangle_{t_0} \tag{1}$$

where $I(t_0)$ and $I(t_0 + t)$ are the speckle intensities of each camera pixel at times $t_0$ and $t_0 + t$, and $<>_{\text{pixels}}$ and $<>_t$ indicates the spatial and temporal averaging over all pixels of the speckle pattern and over the acquisition time respectively. Next, the mean square displacement (MSD) of scattering particles governed by the viscoelastic properties of the local environment was deduced from $g_2(t)$ according to Eq. (2) [17,33–37]:

$$g_2(t) = exp\left(-2\gamma\sqrt{k_0^2 n^2 \left\langle \Delta r^2(t) \right\rangle + \frac{3\mu_a}{\mu_s'}}\right) \tag{2}$$

where $k_0$ is the wave number in vacuum, $n$ is the refractive index of medium, $<\Delta r^2(t)>$ is the MSD of light scattering particles, $\mu_a$ and $\mu_s'$ are the optical absorption coefficient and reduced scattering coefficient respectively, and $\gamma$, generally assumed to be 5/3, is related to the sample optical properties for a fixed illumination/collection setup and sample geometry [17]. The value of $n$ was 1.34 for the PEG and PA hydrogels primarily composed of water, and was equal to 1.44 for PDMS gels based on the product specification. The gels tested in this study were prepared using a strongly scattering media with negligible absorption given the high concentration of titanium dioxide and intralipid scatterers. Therefore, for the purpose of this study, $\mu_a/\mu_s'$ reduced to zero. Additionally, with $\mu_s'$ maintained at 5 mm$^{-1}$, the scattering coefficient was equal to, $\mu_s = \mu_s'/(1\text{-}g) > 15$ mm$^{-1}$ ($g \sim 0.7$). Therefore, the distance between scattering events, $l$, was much smaller than the diffuse mean free path, $l^*$, and on average several scattering events occur per $l^*$. These conditions were conducive for sufficient light diffusion to occur enabling the accurate quantification of the MSD using Eq. (2) above. In the current study we applied intraluminal LSR to evaluate homogeneous phantoms with fairly identical optical properties. We have however, previously shown that LSR also can be applied for investigating the viscoelastic moduli of heterogeneous tissues, biofluids and hydrogels [8–11,13–16,22–24], as long as the sample is homogeneous over a sufficient length scale in order to allow light diffusion to occur through multiple scattering events ($l<<l^*$) within the illuminated volume.

The viscoelastic modulus was obtained by substituting the MSD derived from the $g_2(t)$ into the well-established generalized Stokes-Einstein relation (GSER) [7,18,19,38–41]:

$$G^*(\omega) = \frac{K_b T}{\pi a \left\langle \Delta r^2(1/\omega) \right\rangle \Gamma(1+\alpha(\omega))} \tag{3}$$

where $K_B$ is the Boltzmann constant, $T$ is the temperature in Kelvin, $a$ is the particle radius, $\alpha(t) = \partial\log(<\Delta r^2(t)>)/\partial\log(t)$ is the logarithmic derivative of the slope of the MSD at $\omega = 1/t$, and $\Gamma$ represents the gamma function. For purely viscous materials the MSD increases

linearly with time. However, in the case of viscoelastic materials the displacements of scattering particles are no longer purely diffusive and exhibit a more complex behavior as evidenced in the MSD curves as: $<\Delta r^2(t)> \sim t^\alpha$ [Fig. 3(a)] [13,15,18,38,39,41]. The scattering particle radius, $a$, quantified using a dynamic light scattering instrument (Zetasizer, Malvern Instruments) was 113.5 nm for intralipid and 475 nm for $TiO_2$ particles. For applications in tissue with unknown particle sizes, we have previously shown that average particle radii can be derived from the azimuth intensity profile of time-averaged speckle intensities [42].

To evaluate and visualize spatially-varying differences in sample mechanical properties, the filtered time-varying speckle images (as above) were divided into overlapping 40x40 pixels regions (50% overlap), each covering a few speckle spots. The windowed speckle patterns were used to derive the speckle intensity autocorrelation $g_2(t)$, mean square displacement MSD, and viscoelastic modulus $G^*(\omega)$ as detailed above. To obtain smooth maps of viscoelastic moduli, the discrete value of $|G^*(\omega)|$ of windowed speckle sequences were bi-linearly interpolated. Then the $|G^*(\omega)|$ maps obtained for each channel at each pull-back location were stitched to form a continuous 2D $|G^*(\omega)|$ map for each channel.

## 3. Results

Figure 3(a) shows the average $g_2(t)$ curves for the 3 different gel materials measured by the LSR catheter; the error bars indicate the standard deviations of measurements at 8 locations for each gel compartment. Since the optical properties are identical, the differences in $g_2(t)$ trends were primarily due to differences in sample viscoelastic properties. For instance, the $g_2(t)$ curve corresponding to the softest PEG gel exhibited a significantly faster decay with a lower plateau level compared to the curves representing the moderate PA gels and the stiffest PDMS gels. These observations agreed with the results of conventional mechanical rheometry that showed the $|G^*|$ of the softest PEG gels was 18 Pa, compared to the moduli of 77 Pa
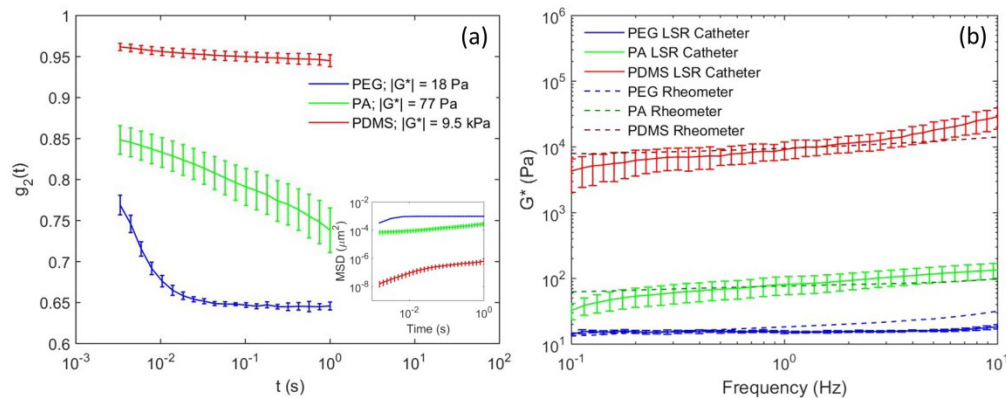


Fig. 3. (a) Speckle intensity autocorrelation curves of the PEG gel, the PA gel and the PDMS gel, obtained using the intraluminal LSR catheter. The softest PEG gel undergoes the most rapid speckle decorrelation compared to the stiffer PA and PDMS gels. The calculated MSDs of the PEG, PA and PDMS gel are plotted in the inset. The MSD of the PEG gel grows rapidly and to a much larger extent than the PA and PDMS gels. (b) Frequency-dependent viscoelastic moduli, $|G^*(\omega)|$, extracted from $g_2(t)$ curves and MSD curves in (a). The viscoelastic moduli for the 3 gel materials measured using a conventional rheometer are shown as dashed curves. Good agreement rheometer can be find between $|G^*(\omega)|$ measured via LSR and those measured via conventional mechanical over a frequency range of 0.1 – 10Hz, with the best correspondence at ~1 Hz.

and 9.5 kPa measured for the PA and PDMS gels respectively (at a frequency of 1Hz). The time-resolved MSD trends for the 3 different gels are shown in the inset of the Fig. 3(a). Clearly, given the rapid Brownian diffusion of light scattering particles, the MSD measured for the PEG gel grew larger with time in comparison to PA and PDMS gels [18,19,38–41].

Figure 3(b) shows the trends of the frequency dependent viscoelastic moduli, $|G^*(\omega)|$, of the 3 gel materials measured using the LSR catheter and computed using Eq. (3) (solid lines), compared with the corresponding measurements obtained using the standard rheometer (dashed lines). We observed $|G^*(\omega)|$ trends for the 3 gels measured by the LSR catheter were in close agreement with those measured by mechanical rheometry over a frequency range of 0.1-10 Hz. To quantify the correspondence between $|G^*(\omega)|$ measured by LSR and mechanical rheometry, we conducted linear regression analysis and paired t-tests at several discrete frequencies between 0.1 and 10Hz. We observed that in all cases, $|G^*|$ measured by LSR was highly correlated with mechanical rheometry with an R-value > 0.84 (p<0.0001) at any frequency within the 0.1-10Hz range. At frequencies between 0.5 and 5 Hz, linear regression results showed an even stronger correlation (R-value > 0.93 (p<0.0001)). Furthermore, the results of t-tests showed that within this frequency range the differences between LSR and mechanical rheometry were not statistically significant (*p*>0.05), with the highest p-value (*p* = 0.31>0.05) observed at a frequency of 1 Hz. In other words, at a frequencies between 0.5 and 5Hz, $|G^*|$ measured by LSR were statistically identical to standard rheometry, at at 1Hz the equivalence was closest. At the high oscillation frequencies mechanical rheometry failed to accurately measure $G^*(\omega)$, due to the emergence of instrument inertia; therefore standard rheometry was restricted to a frequency limit of 10Hz [12,13,43].
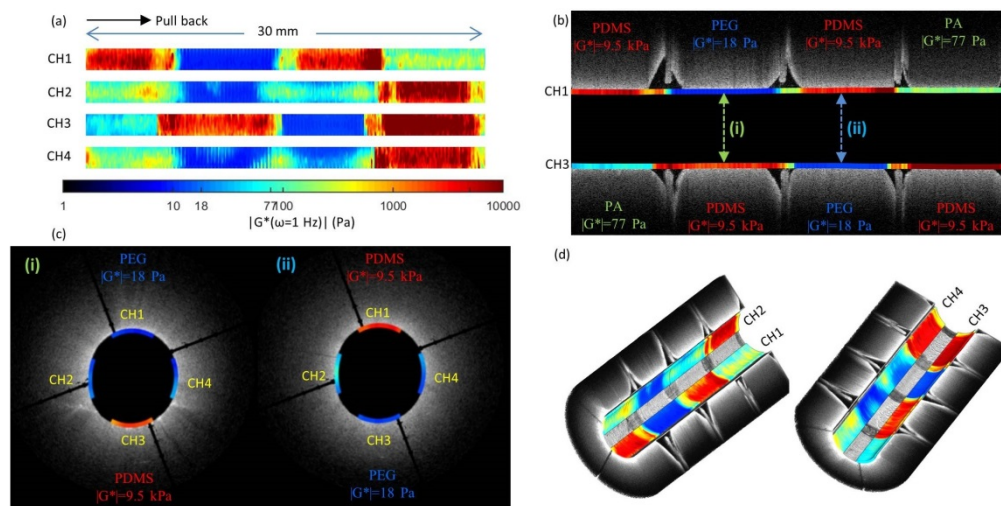


Fig. 4. (a) The four reconstructed 2D maps of $|G^*|$ at 1 Hz for the 4 channels that image the top (CH1), bottom (CH3), left (CH2) and right (CH4) gel compartments of phantom. The arrow shows the catheter pull-back direction over a ~30 mm length of the phantom lumen. The color from black to red indicates $|G^*|$ values measured via LSR ranging from 1 Pa to 10 kPa. Even minute inhomogeneities in mechanical properties within each gel compartment can be detected, demonstrating the sensitivity of LSR for micromechanical mapping using the omni-directional catheter. (b) The longitudinal and (c) the cross-sectional OCT images (grayscale) fused with LSR $|G^*|$ maps (colored). The green and blue arrow lines indicate the longitudinal positions of the cross-sectional images in (c). The LSR $|G^*|$ maps co-registered with the OCT image sections show distinct differences in mechanical properties in accordance with the placement of the different gel compartments. (d) The cutaway views of the 3D volume rendered OCT data with corresponding $|G^*|$ maps overlaid on the luminal surface. The OCT images for the gels in different cells are indistinguishable given similarities in optical properties, while strong mechanical contrast between the $|G^*|$ maps for different gels are observed, demonstrating the capability of LSR for mechanical characterization.

Next, to evaluate the utility of the LSR catheter to visualize spatially varying differences in mechanical moduli, spatio-temporal analysis of the speckle time series was performed at each pullback location. Two dimensional (2D) maps of viscoelastic moduli $|G^*|$ were

visualized [Fig. 4(a)] at the frequency of 1 Hz at which the equivalence between LSR and rheometry is the greatest (based on the results of paired t-tests as above). In Fig. 4(a), the distinct differences of |G*| measured via LSR between each of the gel compartments can be clearly demarcated from the LSR color maps. It was observed that the color maps of $|G*(\omega)|$ measured for CH1 and CH3 accurately followed the tiled arrangement of the gels in the top and bottom layers of the test phantom. More specifically, while the blue tiles corresponded to the softest PEG gel (18 Pa @ 1 Hz measured via standard rheometry), the green tiles matched with the site of PA gel, exhibiting medium stiffness values (77 Pa @ 1 Hz). Moreover, the red tiles were consistent with the locations of the stiffest PDMS gel (9.5 kPa @ 1 Hz). We further observed that the |G*| values, color-coded within the 2D maps, were in close agreement with those measured using the standard mechanical rheometer. Furthermore, within each gel compartment, variations in |G*| could be clearly visualized at high spatial resolution, demonstrating the capability for intra-luminal quantification of distinct micro-mechanical features. In Fig. 4(b) and 4(c), we show representative longitudinal and cross-sectional images of the fused OCT and LSR data. The cutaway views of the 3D OCT data set fused with the cylindrical LSR maps of |G*| are shown in Fig. 4(d). Given the identical light scattering properties the gel materials were indistinguishable in the OCT images. In contrast, given its capability to measure mechanical contrast from speckle intensity fluctuations, LSR could accurately identify gel compartments with distinct differences in viscoelastic moduli, with CH2 and CH4 measuring viscoelastic moduli of the transition regions between the top and bottom gel compartments. Taken together, the above results established the capability to accurately measure the viscoelastic moduli of luminal organs using a novel omni-directional catheter-based LSR approach.

## 4. Discussion

We have described a new approach for conducting intraluminal LSR and have tested its capability for quantifying the frequency-dependent viscoelastic modulus, $G*(\omega)$, of a novel cylindrical gel phantom. By circumventing the need for catheter rotation, this new LSR approach may permit comprehensive intra-luminal evaluation, while reducing the influence of motion artifacts on LSR results.

   The studies conducted using a test luminal phantom demonstrated that the omni-directional catheter could accurately quantify frequency-dependent mechanical moduli as evidenced by the close agreement between the catheter-based measurements and those obtained via mechanical rheometry as shown in Fig. 3, with the closest correspondence observed between 0.5 and 5Hz. The upper frequency limit was restricted by the onset of inertial effects in mechanical rheometry. With increasing oscillation frequency, the penetration depth of the shear strain wave induced by the rheometer tool decreases and inertial effects dominate causing erroneously high values of |G*| measured by the rheometer [43]. In most cases, this usually corresponds to the upper frequency limit of 5-10 Hz, with softer materials exhibiting inertial effects at lower frequencies. These effects may explain the differences observed in $G*(\omega)$ trends of LSR and mechanical rheometry with increasing frequency particularly for the softest PEG gel (Fig. 3(b)) [43].

   Although ILSR measurements spanned a 100Hz frequency range, owing to the lack of a standard reference mechanical tool for high-frequency operation, the accuracy of LSR measurements beyond 10 Hz could not be fully assessed. However, the frequency range of |G*| accessible to LSR is significantly larger than that of mechanical rheometry [7,18]. In LSR, the movement of scattering particles shears the surrounding medium and the inertial effects dominate when the penetration depth of shear waves becomes comparable to the scattering particle size. The small size of the micron-sized scattering particles in LSR, compared to the large gap between rheometer plates, delays the onset of inertial effects to above 1 MHz, thus in principle opening an extended window of frequencies to assess viscoelastic behavior [7,13,15,16]. In practice, these higher frequencies may be achieved in

LSR by employing a CMOS camera that permits speckle pattern acquisition at high frame rate and finer temporal resolution. In the current study, the frame rate of the camera is 300 fps, limiting the highest frequency to ~100 Hz. By employing acquisition speeds, for instance in the order of few 100 kHz, higher frequencies, in the order of $10^5$ Hz may likely be achieved. The unique capability to quantify tissue moduli over a large frequency range will likely provide new insights on the frequency-dependent behavior of tissue under pathological and normal conditions, potentially improving diagnostic yield.

The small, albeit statistically insignificant variations observed between ILSR and mechanical rheometry within the over-lapping frequency range (Fig. 3(b)) are likely caused by differences in the mechanisms of operation of between both techniques. To quantify $G^*(\omega)$ using ILSR, we calculated the MSD of light scattering particles from the speckle intensity autocorrelation, g2(t), by assuming a richly and homogeneously scattering sample medium. In reality however, small local heterogeneities in light scattering properties may occur through the volume of the gel. Within such scattering heterogeneities, light propagation may not be strictly diffusive, resulting in slight variations in estimating the MSD. The fewer light scattering events in local heterogeneities likely elicit slower speckle fluctuations and hence may result in a slight over-estimation of $|G^*(\omega)|$. This may explain why $|G^*(\omega)|$ measured via LSR for PDMS and PA gels are slightly higher than the $|G^*(\omega)|$ curves measured via the conventional rheometry at frequencies above 1Hz (Fig. 3(b)). On the flip side, the mechanical rheometer may cause a slight underestimation of sample mechanical moduli likely due to breakdown the gel structure during shearing. Slight discrepancies at lower frequencies may be likely due to extraneous speckle fluctuations induced by residual low-frequency drifts of the catheter tip over longer durations. The subsequent speckle decorrelations and lower g2(t) plateau level at long times, translate into slightly smaller $|G^*(\omega)|$ values at low frequency, particularly in stiff samples. By selecting optical fiber bundles with diminished cross-talk between neighboring cores, temporal speckle intensity drifts due to the slow motion of the catheter tip may be diminished to improve the accuracy for mechanical characterization.

In this study, OCT is used purely to visualize the morphology of the gel phantom. Prior studies have reported on the use of OCT elastography methods to measure the mechanical properties of samples [44–46]. The fundamental difference between OCT and LSR is that the former relies on single scattering or a very small number of light scattering events, while LSR quantifies laser speckle fluctuations caused by multiple light scattering. Since the photons in LSR undergo a large number of scattering events, an individual light scattering particle needs to displaced only by a fraction of a wavelength for a large cumulative change in the path length to occur to significantly modulate the speckle intensity [47–52]. Thus LSR can measure scatterer displacements of sub-nanometer length scales, providing high sensitivity in detecting passive Brownian motion. On the other hand, in passive approaches that utilize single scattering (such as in OCT) a substantially larger displacement of particles (tens of nanometers) is required to induce a detectable path length change and therefore the minute passive Brownian motions that may occur in stiffer samples are not easily detectable [17,18]. As a result, active modulation approaches are employed in OCT to increase the detectable range of particle MSD via the application of mechanical, acoustic or electromagnetic forces [45,46,53–57]. An advantage of OCT compared to LSR however is the capability for depth-sectioning which provides the opportunity to detect mechanical heterogeneities over a depth of 1-2 mm in tissue. Taken together, both LSR and OCT elastography (OCE) are research tools to measure the mechanical properties of turbid materials such as tissues, with unique advantages and limitations. The high sensitivity of LSR that leverages multiple light scattering allows mechanical characterization using a passive rheology approach via an easy to develop, low-cost optical set up, at the cost of losing depth-sectioning information. On the other hand, OCE provides high-resolution, depth-sectioned maps of sample mechanical properties, albeit at the cost of increased instrument complexity via the use of active modulation strategies.

A current limitation of LSR however is the lower pull-back speed compared to OCT. In this study, time-varying speckle patterns were recorded for 2s resulting in a total imaging time of 7.5 minutes to evaluate a ~3 cm long lumen. The trends of the speckle autocorrelation curves, $g_2(t)$ plotted in Fig. 3, however show that the time scale of speckle fluctuations is significantly shorter (<0.5 s) than the 4 s imaging duration particularly for the two softest phantoms. Furthermore, extracting $|G^*|$ at 1 Hz only requires a maximum effective imaging duration of 0.159 s for each speckle time sequence. Thus, the total imaging time can be significantly reduced to 1min or less to comprehensively characterize the entire 3 cm lumen length. Limiting the need for illumination switching may further reduce imaging time. An alternative approach may be used by illuminating adjacent mirror facets using different wavelengths and recording speckle patterns via dichroic detection, therefore avoiding the influence of speckle image overlap in the measured autocorrelation data.

Our current omni-directional LSR catheters utilize 4- and 6-faceted MFPM with circumferential coverages of 59% and 89% respectively. One way to further increase the FOV coverage for full circumferential viewing is by utilizing a miniaturized cone mirror. Replacing the MFPM with a cone mirror in the distal optics however introduces astigmatism caused by a curved surface of the reflecting cone. One effective way to reduce astigmatism is using a small-diameter aperture to block deviant rays of light, or by applying a double telecentric optical system to reduce optical aberrations. The drawback of these approaches however is that total rigid length at the distal optics will be longer than using only a single lens, and the assembly process will be more complicated. While larger catheters or endoscopes (> 3mm in diameter) may benefit from using the cone mirror approach to improve circumferential FOV coverage, the 4- or 6-faceted MFPM described in the current study are more suitable for smaller diameter LSR catheters albeit at a cost of slightly reduced FOV coverage. Another important issue related to the FOV is the location of the LSR catheter within the lumen. In the current phantom studies, the LSR catheter is aligned at the center of the phantom lumen. However, during *in vivo* use, the position of the LSR catheter may vary or drift relative to the lumen wall during catheter pull-back, altering the FOV in variable ways. Additional methods may be employed that track the effective speckle pattern size to calibrate and monitor catheter position in real time during pull-back. For certain gastrointestinal imaging applications, the LSR catheter may be centered within an inflated balloon to prevent FOV variations relative to the lumen wall during pull-back.

A critical component that influences the quality of the recorded speckle data is the OFB, which is an important limiting factor for further miniaturization of the catheter. The OFB with thousands optical cores offers the advantage of collecting several thousand speckle spots for sufficient optimal averaging thereby reducing the imaging duration of the procedure. Currently, the OFB used in this study incorporates approximately 3500 optical cores within a 550 μm diameter bundle and receives image data comprising several speckle spots. Alternatively, a single SMF may be considered which may reduce fabrication complexity and overall catheter size. The drawback of this alternative approach however, is that since fewer speckle spots are recorded, longer imaging durations will be required and time-averaging over several $g_2(t)$ curves evolving in time will need to be conducted to ensure sufficient ensemble averaging for accurate viscoelastic determination.

Speckle decorrelation may also be caused by the motion of scattering particle due to gradients in temperature, pressure or catheter motion. The absence or near-absence of such convective motions is a necessary condition to accurately distinguish and quantify the MSD of particles caused purely by passive Brownian motion. In many medical applications the time scales of convective motion and passive Brownian motion often distinct, allowing the opportunity for LSR evaluation. For instance, for intracoronary LSR in living animals we have previously demonstrated that speckle image acquisition can be performed at a high imaging rate of >1 kHz which allows sufficient isolation of early Brownian displacements that occur at kHz frequencies from bulk tissue motions that occur at a significantly lower

frequency of 0.5-10 Hz (due to heart beat or respiration) [11]. Alternatively if there is a need to specifically measure lower frequency mechanics, speckle image capture may be gated to the EKG and/or respiratory cycle. For gastrointestinal imaging applications, an intraluminal balloon can be deployed to further reduce effects of low frequency peristaltic motion [58]. In several other applications (such as breast biopsies, cartilage imaging etc.), LSR can be conducted via a small bore needle and effects of pressure gradients during needle insertion may be avoided by delaying speckle image capture by a few seconds following insertion. In the future, ILSR may be conducted to evaluate the coronary vasculature in conjuction with saline flushing to purge blood from the imaging field similar to intracoronary OCT.

## 5. Conclusion

In conclusion, we demonstrate the capability of a new omni-directional viewing catheter that may be useful for the biomechanical profiling of a number of pathological processes for several clinical and research applications. The current catheter is less than 1.2 mm in diameter and is comparable in size to commercially available intravascular catheters and considerably smaller than several gastrointestinal endoscopes, opening the opportunity for LSR evaluation in luminal organs or deep tissues via small diameter endoscopes, catheters or needles.

## Funding

## Acknowledgments